






Ferroelectricity modulates polaronic coupling at multiferroic interfaces

Marius Adrian Husanu ^{1,2✉}, Dana Georgeta Popescu², Federico Bisti^{1,3}, Luminita Mirela Hrib², Lucian Dragos Filip ², Iuliana Pasuk², Raluca Negrea², Marian Cosmin Istrate², Leonid Lev^{1,4}, Thorsten Schmitt ¹, Lucian Pintilie ², Andrey Mishchenko⁵, Cristian Mihail Teodorescu² & Vladimir N. Strocov ^{1✉}

Physics of the multiferroic interfaces is currently understood mostly within a phenomenological framework based on screening of the polarization field and depolarizing charges. Additional effects still unexplored are the band dependence of the interfacial charge modulation and the associated changes of the electron-phonon interaction, coupling the charge and lattice degrees of freedom. Here, multiferroic heterostructures of the colossal-magnetoresistance manganite $\text{La}_{1-x}\text{Sr}_x\text{MnO}_3$ buried under ferroelectric BaTiO_3 and $\text{PbZr}_x\text{Ti}_{1-x}\text{O}_3$ are investigated using soft-X-ray angle-resolved photoemission. The experimental band dispersions from the buried $\text{La}_{1-x}\text{Sr}_x\text{MnO}_3$ identify coexisting two-dimensional hole and three-dimensional electron charge carriers. The ferroelectric polarization modulates their charge density, affecting the coupling of the 2D holes and 3D electrons with the lattice which forms large Fröhlich polarons inherently reducing mobility of the charge carriers. Our k -resolved results on the orbital occupancy, band filling and electron-lattice interaction in multiferroic oxide heterostructures modulated by the ferroelectric polarization disclose most fundamental physics of these systems needed for further progress of beyond-CMOS ferro-functional electronics.

¹Swiss Light Source, Paul Scherrer Institute, 5232 Villigen-PSI, Aargau, Switzerland. ²National Institute of Materials Physics, Atomistilor 405A, 077125 Magurele, Romania. ³Dipartimento di Scienze Fisiche e Chimiche, Università dell'Aquila, Via Vetoio 67100 L'Aquila, Italy. ⁴Moscow Institute of Physics and Technology, 141700 Dolgoprudny, Russia. ⁵RIKEN Center for Emergent Matter Science (CEMS), 2-1 Hirosawa, Wako, 351-0198 Saitama, Japan. ✉email: ahusanu@infim.ro; vladimir.strocov@psi.ch

The proximity of the hole-doped manganite $\text{La}_{0.7}\text{Sr}_{0.3}\text{MnO}_3$ (LSMO) and a ferroelectric (FE) material with a well-defined orientation of the FE polarization (\mathbf{P}), provides a local tuning of the doping level close to the interface^{1,2}. Charge modulation in the interfacial region of LSMO occurs in order to compensate for the unscreened depolarizing field due to the discontinuity in the ferroelectric polarization^{3–5}, with its spatial localization related to the Thomas-Fermi screening length⁶. An electrostatic picture of compensating the FE polarization assumes a charge depletion in LSMO when \mathbf{P} points towards the interface, and a charge accumulation when it points in the opposite direction^{2,7,8}. However, the final picture of the interface-altered electronic structure extends beyond electrostatic-derived arguments. Firstly, the Schottky barrier height between the two joining materials and the FE state control the band alignment and band bending at the interface, and thus the transfer of electrons and holes accounting for compensation of the FE phase^{3,4,9,10}. Then, the orbital and lattice degrees of freedom (DOF) come into play when strain^{11,12} in conjunction with ferroelectric-like distortions⁵ and octahedral tilts¹³, propagating into the interfacial region, modulate the Mn-O bond lengths as compared to the bulk. By lifting orbital degeneracy, it changes the orbital-dependent charge occupations and itinerancy of the carriers^{7,8,14}.

The coupling between the charge and lattice DOFs expresses the polaronic nature of the propagating electron/hole, dressed by the local lattice distortion in the form of a phonon cloud. Such coupled charge-lattice quasiparticles explain the superconductive pairing mechanism¹⁵, the transition from high to low mobility in colossal magnetoresistance materials¹ and the strong charge localization close to the metal-to-insulator transition in Mott insulators^{16,17}. Hence, understanding how electron-phonon interaction (EPI) renormalizes the electron and hole effective mass (m_{eff}) and therefore their mobility is essential for pushing forward oxide electronics beyond the known paradigms. However, addressing the impact of EPI on the interface electronic structure is experimentally challenging since most spectroscopic techniques, by probing the whole heterostructure depth, can rarely isolate the contribution of the contact region only. One way of extracting such information is from the spectral function, $A(\mathbf{k},\omega)$ ¹⁸, which contains the effect of all many-body (electron-electron and electron-boson) interactions. It is directly accessed by angle-resolved photoelectron spectroscopy (ARPES), with the EPI signature being a dip-hump structure of $A(\mathbf{k},\omega)$ accompanying the quasiparticle peak (QP) at low band filling and kinks in the experimental band dispersion^{18,19} at large occupations of the conduction band. Our study uses soft X-ray ARPES^{20,21}, whose probing depth matches the interfacial region and whose sharp intrinsic resolution in the out-of-plane momentum k_z allows precise sampling of the 3D \mathbf{k} -space, to access electronic properties of the LSMO interface buried under thin FE layers of BaTiO_3 (BTO) and $\text{PbZr}_{0.2}\text{Ti}_{0.8}\text{O}_3$ (PZT), which propagate the hole-depletion state into the joining LSMO region. We reveal aspects, which so far remained hidden due to either the extreme surface sensitivity and consequently large k_z broadening²⁰ of conventional ultra-violet ARPES, or the angle-integrated nature of the transport measurements¹⁴, X-ray photoelectron spectroscopy^{4,10,4,10} and X-ray absorption spectroscopies^{1,2,7,14}, previously used to probe such interfaces.

Our results establish the coexistence of hole-coupled 2D and electron-coupled 3D Fröhlich polarons (FP) in LSMO. We show that the polaronic-coupling strength can be tuned by the FE polarization through the preferential occupation of the $e_g(3z^2-r^2)$ orbitals vs $e_g(x^2-y^2)$ ones. Such altered orbital occupation modifies in turn the relative electron/hole density and changes their contribution at the screening of the electron-phonon coupling. In addition, we resolve the subtle balance between hole depletion and

electron accumulation which stabilize the well-defined polarization state of the FE top layer in multiferroic heterostructures.

Results and discussion

The essential aspect of our experiments is the preparation of multiferroic heterostructures, where the FE layer is thin enough to access the electronic structure of the buried interface with soft X-ray photoemission, and at the same time stays above the critical thickness of ~ 3 – 6 unit cells at which PZT and BTO lose their FE character^{5,22}. Such thin FE films, epitaxially grown and strained at the in-plane lattice constant of the substrate, stabilize as a single FE domain due to their high coercive field in the 250 – 350 kV cm^{-1} range^{23–25}, which increases at low temperatures^{26,27}. \mathbf{P} pointing either towards (\mathbf{P}^-) or away from the interface (\mathbf{P}^+)⁵ are opposed by the corresponding depolarizing field and compensated by the modulation of the LSMO charge carriers. Other possible extrinsic mechanisms such as adsorption of polar molecules at the FE surfaces may also have a contribution in stabilizing the ferroelectric state^{27,28}. Additional details on the FE state of the top layers are presented in Supplementary Note 1 and Supplementary Fig. 1.

The combined high leakage currents and high coercive field of the 3 nm-thin FE layers means that in-situ switching of the ferroelectric state between two opposed states $\mathbf{P}^-/\mathbf{P}^+$ is extremely challenging. We will focus instead on comparing the signature of the bare LSMO surface, unmodified by the proximity effect of FEs with the \mathbf{P}^- interface which is stabilized by the LSMO substrate. We note that the probing depth in our soft X-ray ARPES experiment exceeds the thickness of the possibly appearing magnetic dead layer at the LSMO surface, which lies in the 3 unit cells range²⁹. Hence, our approach still correctly delivers information on the spin-integrated intrinsic electronic structure of strained LSMO. We will follow the gradual evolution of charge density and orbital order induced at the interface by ferroelectrics with different magnitude of \mathbf{P} ; with $\mathbf{P}_{\text{BTO}} \sim 20$ – 30 $\mu\text{C/cm}^3$ and $\mathbf{P}_{\text{PZT}} \sim 60$ – 80 $\mu\text{C/cm}^3$ ^{22,28}.

Different occupation probabilities of the otherwise degenerate e_g orbitals in half-filled LSMO result from a competition between the substrate-induced strain and breaking of the symmetry at the surface and interface^{11,12}. The strain lowers the crystal symmetry³⁰, and Jahn-Teller octahedral rotations lift the orbital degeneracy^{8,30}. In-plane tensile strain ($c/a < 1$) lowers the energy of the $e_g(x^2-y^2)$ orbitals, increasing their occupation probability, while compressive strain ($c/a > 1$) lowers the energy and increases occupation of the $e_g(3z^2-r^2)$ ones⁸. These effects alter the hopping probabilities between Mn orbitals with the in-plane and out-of-plane symmetries. On the other hand, breaking of symmetry near the surface has been shown to always favor the $e_g(3z^2-r^2)$ occupation^{11,12}. Joining strained LSMO and epitaxially grown FE oxides further modulates the orbital occupation such that \mathbf{P}^- oriented towards the LSMO contact, increases the $e_g(3z^2-r^2)$ occupation, while the opposite \mathbf{P}^+ direction enhances the $e_g(x^2-y^2)$ occupation^{7,8}.

Our LSMO/FE interfaces are prepared in the $\text{LaSrO}|\text{TiO}_2$ sequence, such that the competing strain and termination effects minimize the e_g splitting Δe_g between the $3z^2-r^2$ and x^2-y^2 orbitals¹², with \mathbf{P} oriented towards LSMO to increase occupation of the $e_g(3z^2-r^2)$ states^{7,8}. The details on the growth methodology are given in *Methods* section (Sample growth: Pulsed Laser Deposition).

Electron microscopy images with atomic and chemical resolution in Fig. 1a reveal the sharp $\text{LaSrO}|\text{TiO}_2$ transition sequence from LSMO to PZT, with no intermixing within the sensitivity range of our measurements. The signatures of the substrate-induced strain in X-ray diffraction and large area microscopy images of both the $\text{BTO}|\text{LSMO}$ and $\text{PZT}|\text{LSMO}$ interfaces are

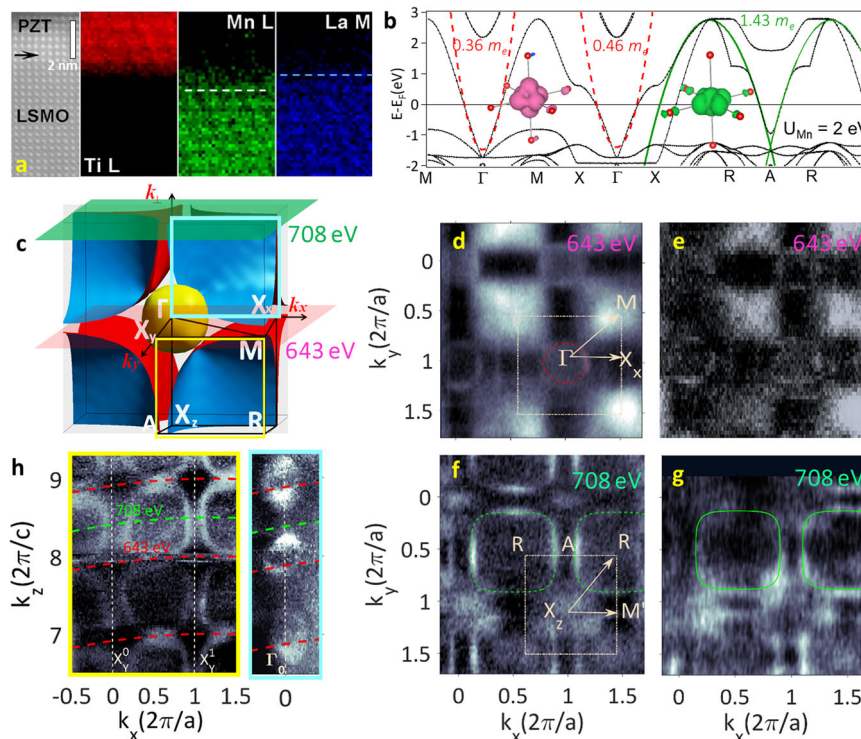


Fig. 1 Structural and electronic properties. **a** High resolution high-angle annular dark-field scanning transmission electron microscopy image at the $\text{PbZr}_{0.2}\text{Ti}_{0.8}\text{O}_3\text{-La}_{0.7}\text{Sr}_{0.3}\text{MnO}_3$ (PZT|LSMO) interface, and Ti L, Mn L and La M maps at atomic level. The black arrow indicates the first ferroelectric unit cell **(b)** Theoretical Hubbard U - corrected density functional theory band structure for SrTiO_3 -strained pseudocubic LSMO and (insets) local density of states integrated ± 0.2 eV around the Γ and A bands bottom. **(c)** Calculated Fermi surface (FS) for strained LSMO. **d, e** In-plane FS maps for respectively bare LSMO and BaTiO_3 (BTO) interface, LSMO|BTO in the ΓMX planes recorded with $h\nu = 643$ eV. **f, g** In-plane FS maps for respectively bare LSMO and BaTiO_3 (BTO) interface, BTO|LSMO in the $X_z\text{AR}$ plane recorded with $h\nu = 708$ eV. **h** Experimental out-of-plane FS maps for the BTO|LSMO heterostructure in the $X_y\text{MR}$ and $\Gamma\text{X}_x\text{Z}$ planes. Colored frames enclosing the out-of-plane FSs encode the probed planes with the corresponding colors from **(c)**.

given in Supplementary Fig. 2 and discussed in Supplementary Note 2.

First-principles density-functional-theory (DFT + U) calculations of LSMO, strained to the in-plane STO lattice constant, are represented in Fig. 1b. They indicate a coexistence of two types of charge carriers at the Fermi level E_F : light electrons and heavy holes. The effective mass of the electrons lying in the $e_g(3z^2-r^2)$ derived 3D bands is $m_{\text{eff}} \sim 0.4 m_e$, where m_e is the free-electron mass. The effective mass of the holes lying predominantly in quasi-2D, $e_g(x^2-y^2)$ derived bands is $m_{\text{eff}} \sim 1.4 m_e$, along the RAR direction of the BZ while the expected m_{eff} along the undispersive directions is expected to be even larger. This makes the overall hole m_{eff} significantly larger than that of the electrons. The effects of correlations and substrate-induced strain on the calculated electronic structure of LSMO are summarized in Supplementary Fig. 4. The corresponding Fermi surface (FS), represented in Fig. 1c is qualitatively similar with previous works and experimental results^{31,32}. It features the 3D electron pocket around Γ , with only a slight mass anisotropy along the ΓM and ΓX directions. These electron states have $e_g(3z^2-r^2)$ character with an admixture of $e_g(x^2-y^2)$. The heavy quasi-2D holes define the FS pocket around the R point, with carriers having predominantly $e_g(x^2-y^2)$ character³¹. The experimental in-plane FS maps recorded at two photon energies $h\nu$ near the ΓXM and $X_z\text{AR}$ planes of the Brillouin zone (BZ) are represented in Fig. 1d, f for bare LSMO and in Fig. 1e, g for the LSMO|BTO heterostructure. Superimposed on the experimental FSs are the calculated FS of the strained LSMO. The out-of-plane FS map in Fig. 1h identifies the 3D character of the LSMO electrons in the 2–3 unit cells close

to the interface. The Luttinger volume³³ of the electron and hole pockets, represented by their areas in the experimental FS cuts, quantifies the corresponding concentrations of electrons (n_e) and holes (n_h). Additional details on the analysis of the ARPES data are given in Supplementary Note 3. Having established the \mathbf{k} -space structure of the electron and hole states, we will now explore the impact of the FE-induced charge density modulation on the concentration and polaronic effective-mass renormalization of the electrons and holes.

FE-induced charge density modulation. First, we will analyze the FE-induced modulation of the charge density represented by the ARPES data. The images in Fig. 2a, b, recorded with 708 eV, represent band dispersions within the cube-like hole pocket along the RAR direction of the BZ for bare LSMO (Fig. 2a) and for the PZT|LSMO interfaces (Fig. 2b). Superimposed on top are the fits of the momentum distribution curves (MDC) maxima through the binding energies (traced by blue dotted line) and the MDCs at E_F (yellow line) whose gradient indicates the Fermi momentum k_F . ARPES images of the BTO|LSMO system recorded in the same conditions are shown in Supplementary Fig. 6. Further details on data analysis are given in Supplementary Note 3. The k_F extraction procedure in several points of the BZ is included in Supplementary Note 3.1 for the hole bands and Supplementary Note 3.2 for the electron bands. The results are presented in Supplementary Figs. 5–7 for the holes and in Supplementary Fig. 8 for the electrons. Table 1 reports the hole densities, calculated using the Luttinger formula³³ from the experimental k_F

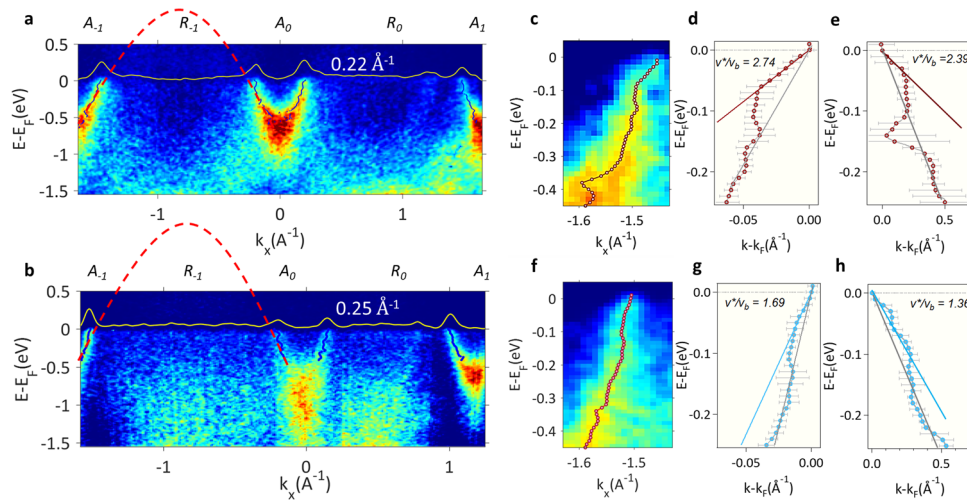


Fig. 2 Quasi-two dimensional hole bands and their dispersion kinks. **a, b** Angle-resolved photoelectron spectroscopy images recorded at the energy $h\nu = 708$ eV and p-polarized light along the RAR direction, probing the hole bands for $\text{La}_{0.7}\text{Sr}_{0.3}\text{MnO}_3$ (LSMO) surface (**a**), and for $\text{PbZr}_{0.2}\text{Ti}_{0.8}\text{O}_3$ (PZT) interface PZT|LSMO (**b**). The dots superimposed on each image are the momentum distribution curve (MDC) maxima, with the MDCs at E_F (yellow lines) used to extract the Fermi wavevector (k_F) values. The dashed lines are guides for the eyes indicating the hole band. **c** Zoom into the low-energy region of the experimental band structure around A_{-1} point for LSMO bare surface. The superimposed dots are the MDC maxima which identifies the kinks in the parabolic dispersion of the hole bands. **d, e** MDC maxima and their linear fits corresponding to the bare and renormalized dispersions in the kink region for LSMO surface interface around two different points of the Brillouin zone: A_{-1} (**d**) and A_1 (**e**). **f** Zoom into the low-energy region of the experimental band structure around A_{-1} point for PZT|LSMO interface. **g, h** MDC maxima and their linear fits corresponding to the bare and renormalized dispersions in the kink region for PZT|LSMO interface around two different points of the Brillouin zone: A_{-1} (**g**) and A_1 (**h**). The error bars represent the standard deviation extracted from the MDC fit with a combination of Lorentz distribution and smooth background.

Table 1 Modulation of carrier concentrations.

		LSMO	LSMO BTO	LSMO PZT
k_F (\AA^{-1})	hole band	0.22 ± 0.08	0.23 ± 0.11	0.25 ± 0.10
	electron band	0.30 ± 0.05	0.35 ± 0.08	0.36 ± 0.07
n (cm^{-3})	hole band	6.42×10^{21}	6.18×10^{21}	5.65×10^{21}
	electron band	0.46×10^{21}	0.75×10^{21}	0.82×10^{21}

Experimental Fermi wavevectors k_F extracted from the momentum distribution curves (MDCs) at the Fermi energy (E_F) for the bands defining the hole and electron pockets, and the corresponding hole and electron densities, n , for $\text{La}_{0.7}\text{Sr}_{0.3}\text{MnO}_3$ (LSMO) surface in comparison with the interfaces with ferroelectrics (FE = $\text{PbZr}_{0.2}\text{Ti}_{0.8}\text{O}_3$ - PZT and BaTiO_3 - BTO), LSMO|FE. The errors express the standard deviation and are extracted from the fit of the MDCs with a combination of Lorentz distribution and smooth background.

values as:

$$n_h = (2\pi/a - 2k_F)^3 / (2\pi)^3 \quad (1)$$

assuming the approximately cubic shape of hole pockets. These results demonstrate that the FE polarization significantly depletes n_h at the LSMO|FE interfaces compared to bare LSMO surface. The gradual decrease of n_h manifests the expected hole-depletion state, induced in the LSMO substrate by the \mathbf{P}^- state of the FE top layer, where the FE field is compensated by carriers from LSMO^{2,4}. This evolution scales with the increasing value of \mathbf{P} in BTO and PZT.

The microscopic mechanism of interface coupling is a combined effect of:

1. charge building up in LSMO close to the interface with the FE in order to compensate the bound FE charges and the resulting depolarizing field, stabilizing the well-defined orientation of \mathbf{P}^9 . This charge depends on both the magnitude of \mathbf{P} and on the amount of intrinsic compensation charges already available in the FE through self-doping mechanisms²⁸. For the same layer thickness ~ 3 nm, the density of free carriers in BTO, with its oxygen vacancy-assisted n-type conduction, exceeds by at least one order of magnitude that of PZT³. Hence, it requires less

compensation charges in the metallic electrode to stabilize the inwards \mathbf{P}^- state. Accordingly, the alteration of the LSMO electronic structure expressed by the experimental n_h values is weaker when interfacing to BTO than to PZT³.

2. FE instability, consisting in off-centering of the cations, modified tetragonality and octahedral tilts in the top layer which propagates into LSMO within the first unit cells, lowering the energy of the e_g orbitals and favoring their preferential occupation⁶⁻⁸. This effect has also been shown to directly scale with the magnitude of \mathbf{P} through the cation displacement with respect to the centro-symmetric configuration, propagating into LSMO. Such instability induced by the PZT layer^{28,34} is at least by a factor of two larger than BTO¹⁴. Consequently, its impact on the electronic structure through the induced displacement of the Mn atoms from the central position, modified tetragonality ratio (c/a) and octahedral conformation is also stronger^{5,8,13}.

For the electron states, the effect of the FE polarization is clear from the ARPES data in Fig. 3. The latter compares the ARPES images for the LSMO|PZT interface and bare LSMO recorded at the Mn $2p$ resonance in the ΓX direction. These images represent band dispersions for the $e_g(3z^2-r^2)$ derived electron pockets centered at the Γ point (Fig. 1d-f) through two BZs. The experimental k_F values and the corresponding electron densities, evaluated assuming approximately spherical shape of electron pockets and also presented in Table 1, and show the increase when going from LSMO to the buried LSMO|PZT interface (Fig. 1d). The ARPES images for the LSMO|BTO interface are shown in Supplementary Fig. 8. Therefore, the FE polarization oriented inwards (\mathbf{P}^-) results indeed in accumulation of additional electrons in the interfacial region of the LSMO|FE heterostructures compared to the LSMO surface, in agreement with previous experiments^{2,7}. However, our measurements allow for the first time a distinct separation of the electron and hole contribution to the total FE-induced charge density $n = n_h - n_e$. We will see below that although n_e is significantly smaller than n_h , its increase predominates in

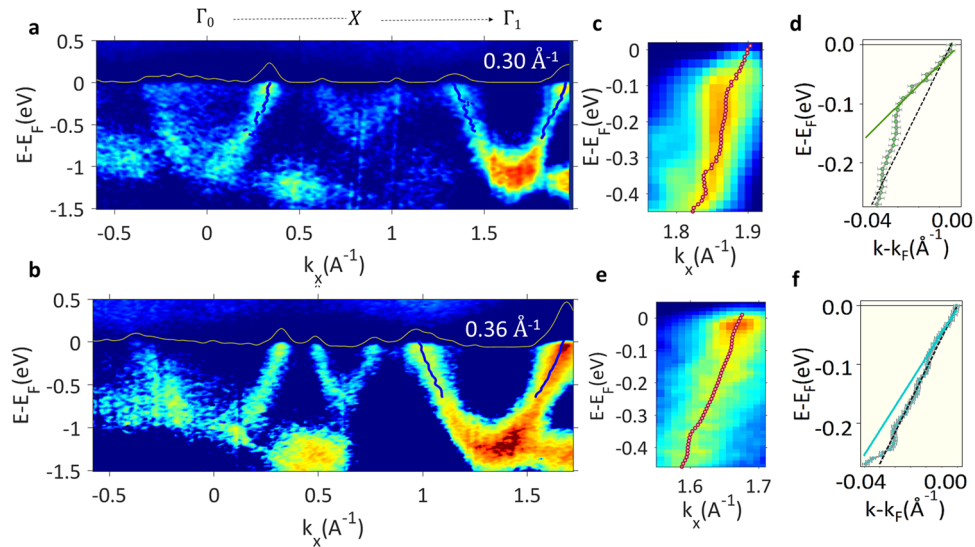


Fig. 3 Three-dimensional electron bands and their dispersion kinks. Angle-resolved photoelectron spectroscopy (ARPES) images recorded with the energy $h\nu = 643$ eV and p-polarized light along the ΓX direction, probing the electron bands for $\text{La}_{0.7}\text{Sr}_{0.3}\text{MnO}_3$ (LSMO) (a) and $\text{PbZr}_{0.2}\text{Ti}_{0.8}\text{O}_3$ (PZT) interface, PZT|LSMO (b). The momentum distribution curves (MDCs) at the Fermi energy (E_F) (yellow lines) are used to extract the Fermi wavevector (k_F) values. (c) Zoom-in of the ARPES images in the low-energy region, with the superimposed red dotted line showing the MDC maxima for LSMO surface. (d) Low-energy MDC maxima and their linear fit corresponding to the bare and renormalized dispersions in the kink region for LSMO surface (d). (e) Zoom-in of the ARPES images in the low-energy region, with the superimposed red dotted line showing the MDC maxima for PZT|LSMO interface. (f) Low-energy MDC maxima and their linear fit corresponding to the bare and renormalized dispersions in the kink region for PZT|LSMO interface (f). The error bars represent the standard deviation extracted from the MDC fit with a combination of Lorentz distribution and smooth background.

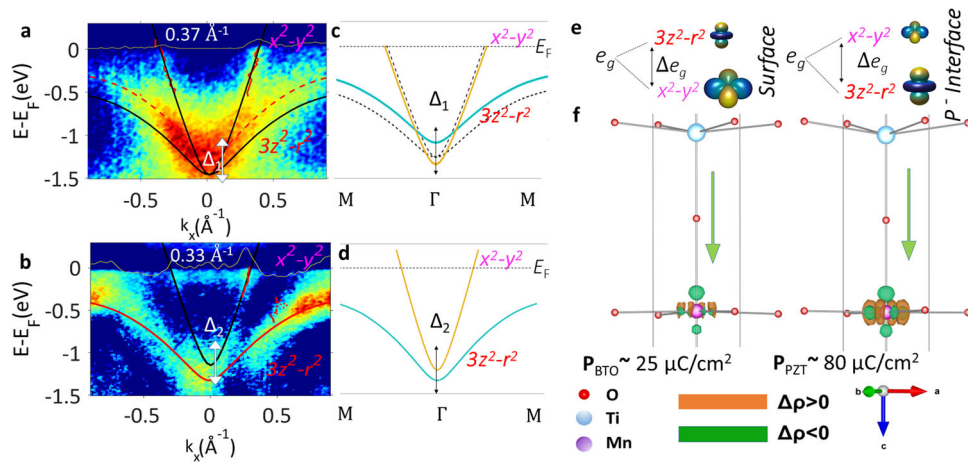


Fig. 4 Orbital polarization. Angle-resolved photoelectron spectroscopy (ARPES) images along the ΓM direction measured at the energy $h\nu = 643$ eV and s-polarized light for (a) $\text{La}_{0.7}\text{Sr}_{0.3}\text{MnO}_3$ (LSMO), and (b) at the $\text{PbZr}_{0.2}\text{Ti}_{0.8}\text{O}_3$ (PZT) interface, PZT|LSMO. The momentum distribution curves (MDCs) at the Fermi energy (E_F) (yellow lines) are used to extract the Fermi wavevectors (k_F s). The superimposed band calculations for strained LSMO are rigidly shifted for PZT|LSMO in order to match the experimental k_F . The splitting between the e_g orbitals of LSMO $\Delta_{1,2}e_g$ in the Γ point measures energy separation of the $(3z^2-r^2)$ and (x^2-y^2) -derived bands. The sketch of the corresponding ARPES dispersions for bare LSMO assuming degenerate e_g orbitals (dotted line) and surface-lifted degeneracy (c) and PZT|LSMO interface (d) is based on the corresponding energies of the $(3z^2-r^2)$ - and (x^2-y^2) orbitals at the surface and at the interface (e). (f) Density functional theory (DFT) slab calculations of the interface charge density for BaTiO₃ (BTO) interface, BTO|LSMO and PZT|LSMO shows how the modulation of charge carrier density in the first LSMO unit cell depends on the magnitude of the inwards P^- polarization.

screening of EPI and corresponding renormalization of the charge carrier's m_{eff} .

Finally, we will analyze the mechanism of FE-induced electron accumulation in terms of atomic orbitals. Fig. 4a, b presents the ARPES images collected along the ΓM direction using s-polarized light. In principle, the dipole selection rules at our experimental geometry suggest that these images reveal only the antisymmetric bands with the $e_g(x^2-y^2)$ character²¹. However, the low-temperature rhombohedral phase of LSMO lacks exact symmetry

planes, and the mixture of domains with 3 different axis orientation^{31,35} relaxes this strict linear dichroism, surviving only at the Γ point. There, the symmetry prevents $e_g(x^2-y^2)$ and $e_g(3z^2-r^2)$ bands from hybridization even under octahedral tilt and rotations³⁵. It was shown⁸ that the FE instability propagating in LSMO alters the ideal overlap of the wavefunctions, their hopping probabilities and bandwidths, with the energy of e_g orbitals varying such that P pointing towards LSMO interface lowers the $e_g(3z^2-r^2)$ energy and increases its occupation, while opposite

orientation of \mathbf{P} increases the $e_g(x^2-y^2)$ occupation. Assuming well-defined orbital character of the bands in the Γ point, the split of our e_g -derived bands, with the $e_g(x^2-y^2)$ -like band shifted towards E_F and consequent smaller k_F at the interface with PZT (Fig. 4b) compared to the bare LSMO (Fig. 4a) is consistent with the mechanism established before⁸. Hence the splitting $\Delta e_g = E[(3z^2-r^2)] - E[(x^2-y^2)]$, between the corresponding bands bottom relates to the different energy of the $e_g(3z^2-r^2)$ and $e_g(x^2-y^2)$ orbitals at our interfaces³⁵. For the bare LSMO surface, the positive $\Delta e_g = 0.18$ eV is a direct indication of the higher energy and thus lower occupation of the $e_g(3z^2-r^2)$ orbital compared to the $e_g(x^2-y^2)$ one^{11,12}. At the interface with PZT, on the contrary, the negative $\Delta e_g = -0.2$ eV indicates the preferential occupation of the $3z^2-r^2$ orbital. The value $\Delta e_g = 0.15$ eV at the BTO|LSMO interface (Supplementary Fig. 8) manifests an intermediate trend, with the relative $e_g(x^2-y^2)$ and $e_g(3z^2-r^2)$ energy only weakly modified by the smaller \mathbf{P} of BTO. This is possibly due to partial relaxation of the BTO layer as revealed by the XRD measurements and consequent decrease of the FE polarization close to the interface. The electron concentrations on the three systems are comparatively presented in Supplementary Table 1. On the theoretical side, our supercell DFT calculations confirm that such changes in the interfacial charge distribution depend on the magnitude of \mathbf{P} . The difference between the charge density of Mn computed between atoms lying at the interface and in bulk $\Delta\rho = \rho_{\text{interface}}^{\text{(SCF)}} - \rho_{\text{bulk}}^{\text{(SCF)}}$ shows that the magnitude of the charge density variation at the LSMO interface scales with the value of the FE polarization (Fig. 4f). More exactly, $\Delta\rho > 0$ indicate additional charge accumulation in the t_{2g} orbitals and charge depletion mostly in the $e_g(x^2-y^2)$ ones. The picture of the FE-dependent band filling of $e_g(3z^2-r^2)$ states (Fig. 4c, d) is consistent with the trend established before in XAS measurements^{7,14}, which identify different relative energies of LSMO e_g states triggered by the FE switch of the top layer (Fig. 4e).

Polaronic effective-mass renormalization. Quasi-2D hole polarons. We will now turn to the analysis of EPI manifested by renormalization of the charge carrier's m_{eff} . The ARPES images in Fig. 2a, b are overlaid by the MDC maxima, identifying the experimental band dispersions of bare LSMO and PZT|LSMO interface. Closely following the theoretical band structure, upon approaching E_F , these dispersions go through a kink, which manifests as a renormalization of the bare bands and corresponding increase of m_{eff} . The kink position in the 40–70 meV range corresponds to the phonon modes active in thin LSMO layers^{30,36,37}. It is reasonable then to assume that the kink origin is in the EPI. We stress that the observed kinks are no artifacts due to energy or \mathbf{k} variations of the ARPES matrix element, but intrinsic properties of the $A(\mathbf{k},\omega)$ spectral function in LSMO as evidenced by qualitatively similar kink structures observed through higher BZs in k_{\parallel} as seen in Fig. 2d, e, g, h and Supplementary Figs. 5–7.

Linear fits of the experimental dispersions in the bare-band and renormalized-band regions below and above the kink, respectively, yield the corresponding Fermi velocities and an estimate for the m_{eff} renormalization.

$$m_{\text{eff}}/m_b = v_F^b/v_F^* \quad (2)$$

Here, m_b and m_{eff} are the bare and renormalized effective masses, and v_F^b and v_F^* are bare and renormalized Fermi velocities, respectively.

The obtained m_{eff} values are compiled in Table 2. The enhancement of m_{eff} by a factor of ~ 3 for bare LSMO's hole band is consistent with the previous reports on epitaxially grown and substrate-strained LSMO from photoemission³², optical

Table 2 Mass renormalization and the electron-phonon interaction (EPI) strength.

		LSMO	LSMO PZT
hole bands	m_{eff}/m_e	3.74 ± 0.42	1.69 ± 0.36
	α^{2D}	3.38	1.05
electron band	m_{eff}/m_e	2.50 ± 0.81	1.30 ± 0.4
	α^{3D}	4.07	1.5

Electron and hole effective masses (m_{eff}) at $\text{La}_{0.7}\text{Sr}_{0.3}\text{MnO}_3$ (LSMO) surface and at the $\text{PbZr}_{0.2}\text{Ti}_{0.8}\text{O}_3$ interface, PZT|LSMO deduced with Eq.(2) from the Fermi velocities obtained in turn by a linear fit of the band dispersions in the kink region. The dimensionless coupling constant $\alpha^{2D,3D}$, estimates the EPI strength for the two-dimensional (2D) hole and three-dimensional (3D) electron Fröhlich polarons. The errors express the standard deviation and are obtained from the individual linear fit of each kink region.

conductivity³⁷ and transport data³⁸. Intriguingly, the experimental m_{eff} decreases under the FE polarization in LSMO|PZT.

It was previously established that the mechanism of EPI in LSMO^{37,38} involves coupling of electrons with optical phonons through long-range Coulomb interaction as captured by the Fröhlich term³⁹:

$$|V_d(\mathbf{q})|^2 \sim \alpha/(q^{(d-1)} + \kappa^{(d-1)}) \quad (3)$$

where α is the dimensionless coupling constant, $d = 2$ or 3 the polaron dimensionality, \mathbf{q} the phonon wavevector, and κ the screening wavevector. Note that a d -dimensional polaron means that the electron is confined in d -dimensional space while the polarization is three-dimensional. This identifies the phonon-coupled charge carriers in the hole band as 2D polarons. For large Fröhlich polarons, the EPI strength is determined by the constant α . Except for extremely weak EPI, there is no analytic expression for α , and evaluation of the polaron properties requires unbiased exact numeric methods such as Feynman's path integral formalism⁴⁰ or Diagrammatic Monte Carlo (DMC)^{41,42}

Based on the experimental m_{eff} , we extracted the corresponding values of α^{2D} (Table 2) from DMC calculations for the 2D case⁴¹ relevant for the hole bands. Whereas for bare LSMO the α^{2D} value lies in the intermediate-coupling regime of EPI, the FE polarization forces the Fröhlich polarons to transition to the weak-coupling regime. Equation (3) shows that this can only be forced by the screening constant κ , which increases with mobile charge density^{18,19}. However, the experimental n_h in Table 1 shows the opposite trend, decreasing under the FE polarization at the LSMO|FE interface. Therefore, an explanation could be that the additional electrons building up in the interface region⁴, play the decisive role in screening of the EPI and undressing the charge carriers from the phonons.

Due to insufficient statistics, the BTO|LSMO analysis of the hole band in terms of renormalized effective mass derived from the fit of the kink region is more challenging, hence we will formulate our conclusions on band renormalization based on the bare LSMO and PZT|LSMO data. However, the BTO|LSMO dataset is enough to establish the interface doping trend from the k_F variation (Table 1), which suggests a transition of the coupling strength to low coupling regime going from the LSMO surface to the \mathbf{P}^- interface.

Polaronic effective-mass renormalization. 3D electron polarons. We will now return to the ARPES data for the $e_g(3z^2-r^2)$ derived electron bands of LSMO surface, presented in Fig. 3a and of the LSMO|PZT interface in Fig. 3b. Their dispersions in the low-energy region, zoomed-in in respectively Fig. 3c, d, show the kink similar to the hole bands. Mapped by the MDC maxima in Fig. 3d for LSMO surface and in Fig. 3f for LSMO|PZT interface, the kink appears at approximately the same energy as in the hole

bands, indicating its origin due to the EPI. Whereas for LSMO the kink and the corresponding renormalization of m_{eff} are distinct, for its interface with PZT they are barely visible. From the linear fit of the band dispersions below and above the kink, we extracted the corresponding Fermi velocities of the bare and renormalized bands for LSMO and the LSMO|PZT interface, which yielded the m_{eff} -renormalization values compiled in Table 2. The kinks around other symmetry-related k_{F} points in Fig. 3a, b show smaller spectral intensity, but yield essentially identical renormalization values. The corresponding coupling parameters α^{3D} , found from the DMC calculations in 3D case⁴², are also given in Table 2. Similarly to the hole bands, the α^{3D} values exhibit a transition from the intermediate coupling regime in LSMO ($\alpha^{3D} \sim 4.1$) to weak coupling at the LSMO|PZT interface ($\alpha \sim 1.5$). This trend signals that the modulation of n_e due to the FE polarization provides better EPI screening. The same trend is identified for the bands dispersing along ΓM direction as seen in Supplementary Fig. 9 and in Supplementary Table 2. Although for BTO|LSMO we could not estimate α^{3D} with enough accuracy, the trend in n_e suggests an α^{3D} value intermediate between those of LSMO and PZT|LSMO.

The electrons attracted by the FE polarization into the interfacial region resolve the above puzzle of why the depletion of the hole charge carriers goes along with the EPI reduction in the hole bands. Such an effect has been observed in other manganites¹⁶ where it was related to the fact that the electrons have much smaller m_{eff} compared to the holes. Being light, they are faster than the lattice oscillation and can therefore screen the EPI much more efficiently compared to the holes, whose m_{eff} in the third dimension is very large¹⁶. Hence, we believe that a similar argument might operate here as well, with the light electrons as the carriers which set the interface to the weak-coupling regime of the Fröhlich polarons. Indeed, the density of light electrons, n_e is smaller by more than one order of magnitude compared to that of the heavy holes n_h , as seen in Table 1. However, the FE-induced increase of the light electron's n_e is enough to drive LSMO from the strong- to weak coupling regime. Moreover, the 3D character of interface electrons (Fig. 1h) suggests that the identified decrease of the polaronic coupling extends into the bulk beyond the Thomas-Fermi screening length¹⁷, implying the concomitant conductivity increase in a region exceeding the sharp interface region.

This is because the distribution of the 3D electrons, deriving from a complex interplay between interface potential and mutual dynamic screening, is not governed by the Thomas-Fermi theory. Hence the light electrons, with their 3D character, presumably spread larger distances from the interface than the Thomas-Fermi length, providing static screening of slow lattice distortions even far from the interface.

Consequently, at the P^- interface we identify the expected electron accumulation and hole depletion, translating into a smaller adimensional polaronic coupling constant. This result indicates weaker electron-phonon interaction at the P^- .

This finding shows that the light electron accumulation/depletion controlled by the FE state of the top material, and the accompanying better/weaker screening of the EPI is the key player in the modulated polaronic coupling at the FE/LSMO interface.

Conclusions

Our k-resolved soft X-ray photoemission results on multiferroic LSMO/BaTiO₃ and LSMO/PbZrTiO₃ heterostructures resolves (A) the missing ferroelectric, band-dependent electron/hole accumulation/depletion induced at the interface, extending the previous understanding of P dependent modulation of orbital energies under FE switch^{7,8}.

Specifically, the FE instability propagating into the interfacial region of LSMO pushes the $e_g(x^2-y^2)$ derived bands defining the hole pockets around the R point, up in energy by ~ 0.2 eV, in accordance with the expected order of the LSMO e_g orbitals at the P^- interface^{7,8}. With the energy of the $(3z^2-r^2)$ orbitals, and their corresponding bands defining the electron pocket bands around the Γ point below the (x^2-y^2) ones, charge accumulation occurs in the former and charge depletion in the latter. This effect further propagates into (B) modulation of the EPI strength, expected changes in conductivity, allowing to tune the functionality of the interface. At relatively small influence of the heavy holes in the x^2-y^2 bands, the fast dynamic response of the light electrons in the $3z^2-r^2$ band effectively screens the EPI. Therefore, the electron accumulation in this band reduces the EPI strength from intermediate for bare LSMO to weak at its interface with the FE overlayer. This regime, with the charge excitations undressed from the lattice vibrations, increases the electron and hole itinerancy. The P^- FE polarization should therefore increase the charge carrier mobility, although this phenomenon still awaits verification in transport experiments, while the opposite FE state, by increasing the EPI strength, should decrease interface mobility. Such an effect of the FE polarization on the renormalization of m_{eff} through the EPI strength, which has escaped identification in the previous works, should be taken into account in functional interfaces between the FE and oxide materials, in addition to the other existing mechanism of FE-assisted enhanced carrier mobility⁴³.

The detailed band-resolved picture disclosed by our results on how the P affects the orbital occupancy, band filling and electron-lattice interaction unveils a number of novel avenues towards further progress not only focused on the multiferroic oxide heterostructures discussed above, but also in the whole vast field of oxide electronics and spintronics. For example, P can be used to tune the mobility of the charge carriers in oxides through modified EPI, in turn modulated by the electron concentration. Particularly promising in this respect are systems where electron correlations increase the population of light-electron bands compared to heavy-hole ones similarly to Ce-doped CaMnO₃¹⁶. The electron correlations themselves can also be tuned through the band filling changing under the FE polarization (electron-correlation engineering). Furthermore, in multiband systems such as LSMO, where 2D charge carriers coexist with 3D ones, the polarization can tune their relative concentration and thus the dimensionality of the overall electron transport. Still to be explored is the oxide FE/superconductor heterostructures, where the polarization could be utilized to change the effective doping and the regime of phonon-mediated superconductivity⁴⁴ through the polarization-induced modulation of the EPI strength identified here for LSMO. Such mechanisms could be used, for example, for realization of switches for power-saving electronics based on Josephson junctions. These ideas open only a few possible novel avenues towards realization of oxide electronic, spintronic, and superconducting devices based on our findings of the multifaceted effect of FE polarization on the orbital occupancy, band filling, electron correlations and electron-boson interaction.

Methods

Sample growth: pulsed laser deposition. Epitaxial LSMO samples were grown on SrTiO₃ (STO) substrates using a thin (5 unit cells) SrRuO₃ (SRO) buffer layer between STO and LSMO. Heterostructures have been prepared by pulsed laser deposition using a well-established recipe to result in epitaxial growth as well as smooth surfaces and sharp interfaces^{3,9,28}.

The FE(3.2 nm)/La_{0.7}Sr_{0.3}MnO₃(20 nm)/SrRuO₃(2 nm)/SrTiO₃ - (FE/LSMO/SRO/STO) and La_{0.7}Sr_{0.3}MnO₃(20 nm)/SrRuO₃(2 nm)/SrTiO₃ (LSMO/SRO/STO) samples were grown on (001) SrTiO₃ single crystals that were first cleaned in buffer solution of hydrofluoric acid (HF) and then annealed in air at 1000°C for 2 h. This

treatment promotes an epitaxial growth of the films with atomic layer precision. The ablation of the FEs, SRO and LSMO targets was performed by using a KrF laser ($\lambda = 248$ nm) and a repetition rate of 5 Hz for SRO and FEs and 1 Hz for LSMO. The laser fluence was 2 J/cm^2 for the deposition of LSMO, SRO and PZT films, and 1.5 J/cm^2 for BTO. The substrate temperature was maintained at 700°C and the oxygen pressure during deposition was 0.14 mbar for BTO and PZT, 0.13 mbar for SRO and 0.27 mbar for LSMO. The as-grown LSMO, SRO and BTO films were post-deposition annealed, in the deposition chamber, at 700°C , for one hour, in O_2 atmosphere while post-annealing of PZT was performed at 575°C to prevent Pb migration. Then, they were transferred in N_2 atmosphere from the preparation chamber to the analysis one, which we notice to bring only a minimum surface contamination easy to overcome by the high probing depth of the soft X-ray range.

SX-ARPES. Experiments were carried out at ADDRESS beamline at Swiss Light Source which delivers high photon flux in soft X-ray range²¹, allowing the band structure investigation of buried interface with the additional benefit of sharp momentum resolution along the out-of-plane direction k_z ²⁰ and thus full 3D momentum. The relationship between electron momentum (k_{\parallel}, k_{\perp}), photoelectron kinetic energy and the photoelectron emission angle²¹ are given in Supplementary Note 3. The geometry of the experimental setup²¹ is such that the incoming s-polarized (p-polarized) photon beam has the electric field oscillating perpendicularly (parallel) to the measurement plane, thus the selection rules of the photoemission process permit to probe only the antisymmetric (symmetric) states with respect to that measurement plane (Supplementary Fig. 3). ARPES measurements have been performed in pressure better than 10^{-10} mbar and a temperature of 12 K. Fermi level is calibrated using a gold foil in electrical contact with the sample. A combined resolution (thermal broadening in addition to the photon beam and the ARPES analyzer) was ~ 70 meV.

Transmission electron microscopy (TEM). Transmission electron microscopy observations have been performed using a probe-corrected analytical high-resolution JEM ARM 200 F electron microscope operated at 200 kV, equipped with a Gatan Quantum SE Image Filter for EELS. Atomic resolution images have been recorded in STEM mode (0.08 nm point resolution) using the High-Angle Annular Dark Field (HAADF) detector. Chemical maps at atomic resolution have been obtained by EELS-SI in the STEM mode. Images and spectral data processing have been made using specialized routines under Gatan Digital Micrograph. For the atomic-resolution spectrum-image experiments the electron beam has been scanned inside a 25 nm^2 across the interface region. The probe dwell time was set at 20 ms/pixel. The chosen convergence angle was 2.6 mrad using a condenser aperture of $30 \mu\text{m}$ diameter, while the collection angle was 18 mrad at 3 cm camera length and for the spectrometer entrance aperture of 2.5 mm. The energy dispersion and the spectral window were set in such a way to allow the simultaneous acquisition of the Ti L, O K, Mn L, Ba L and La M signals.

First-principles calculations. The calculations were performed within the generalized gradient approximation (GGA) using the quantum ESPRESSO plane-wave code^{45,46}, and the exchange-correlation functional in the Perdew–Burke–Ernzerhof (PBE) parametrization. We used norm-conserving pseudopotentials from PseudoDojo⁴⁷. The heterostructure was modeled by a $1 \times 1 \times 14$ supercell geometry starting from the relaxed structure of the LSMO unit cell, but imposing the calculated in-plane lattice constant $a = 3.903 \text{ \AA}$ of SrTiO_3 . This supercell contained 7 unit cells (u.c.) of BTO and PTO in contact with 7 u.c. of LSMO. This thickness ensures that the FE property remains stable, because the FE-polarization states tend to merge starting from a thickness of 5 u.c.⁴⁸. The z-coordinates were allowed to relax until the Hellman-Feynman forces on each atom were less than 2.5 meV/\AA . La-Sr substitutional doping was treated by means of virtual crystal approximation (VCA) replacing each A-site of the perovskite with a fictitious atom with fractional valence, instead of explicit doping which would be computationally expensive due to larger supercells. The VCA generation of the pseudopotential has been checked to reproduce the correct electronic properties of bulk LSMO. The coordinates of the slab are given in Supplementary Data 1. The kinetic-energy cut-off for the plane waves was set at 60 Ry and for the charge density at 240 Ry. The BZ integration was performed on an automatically generated Monkhorst–Pack $3 \times 3 \times 3$ k-mesh, for all slabs, with Gaussian energy-level smearing of 0.02 Ry. For bulk LSMO band structure, a $U_{\text{Mn}} = 2 \text{ eV}$ Hubbard parameter was employed, which reproduces well the half-metallic character of the LSMO.

X-ray diffraction. The lattice parameters of the epitaxial structures have been determined by high resolution X-ray diffraction, using a Bruker D8 Advance X-ray diffractometer with nickel-filtered Cu K α radiation, parallelized with a Göbel mirror. Symmetric scans with miscut correction (2θ - ω scans) were performed to evaluate the structural characteristics perpendicular to the substrate. Reciprocal-space mappings (RSM) around the STO node were performed to confirm the epitaxy on the whole area and thickness of the thin layers, and to estimate the in-plane lattice parameters and the epitaxial strain. The lattice parameters of the thin films were determined using the reflections of the cubic STO substrate ($a = 3.905 \text{ \AA}$) as the reference.

Data availability

All data presented in this work and data processing procedures are available from the corresponding authors upon request.

Received: 27 December 2021; Accepted: 24 July 2022;

Published online: 15 August 2022

References

- Molegraaf, H. J. A. et al. Magnetoelectric Effects in Complex Oxides with Competing Ground States. *Adv. Mater.* **21**, 3470–3474 (2009).
- Vaz, C. A. F. et al. Origin of the magnetoelectric coupling effect in $\text{Pb}(\text{Zr}_{0.2}\text{Ti}_{0.8})\text{O}_3/\text{La}_{0.8}\text{Sr}_{0.2}\text{MnO}_3$ multiferroic heterostructures. *Phys. Rev. Lett.* **104**, 127202 (2010).
- Pintilie, I. et al. Polarization-Control of the Potential Barrier at the Electrode Interfaces in Epitaxial Ferroelectric Thin Films. *ACS Appl. Mater. Interfaces* **6**, 2929–2939 (2014).
- Popescu, D. G., Barrett, N., Chirila, C., Pasuk, I. & Husanu, M. A. Influence of hole depletion and depolarizing field on the $\text{BaTiO}_3/\text{La}_{0.6}\text{Sr}_{0.4}\text{MnO}_3$ interface electronic structure revealed by photoelectron spectroscopy and first-principles calculations. *Phys. Rev. B* **92**, 235442 (2015).
- Peters, J. J. P., Apachitei, G., Beanland, R., Alexe, M. & Sanchez, A. M. Polarization curling and flux closures in multiferroic tunnel junctions. *Nat. Commun.* **7**, 13484 (2016).
- Pruneda, J. M. et al. Ferrodistortive Instability at the (001) Surface of Half-Metallic Manganites. *Phys. Rev. Lett.* **99**, 226101 (2007).
- Preziosi, D., Alexe, M., Hesse, D. & Salluzzo, M. Electric-Field Control of the Orbital Occupancy and Magnetic Moment of a Transition-Metal Oxide. *Phys. Rev. Lett.* **115**, 157401 (2015).
- Chen, H. et al. Reversible Modulation of Orbital Occupations via an Interface-Induced Polar State in Metallic Manganites. *Nano Lett.* **14**, 4965–4970 (2014).
- Tănase, L. C. et al. Polarization Orientation in Lead Zirconate Titanate (001) Thin Films Driven by the Interface with the Substrate. *Phys. Rev. Appl.* **10**, 034020 (2018).
- Rault, J. E. et al. Interface electronic structure in a metal/ferroelectric heterostructure under applied bias. *Phys. Rev. B* **87**, 155146 (2013).
- Tebano, A. et al. Evidence of Orbital Reconstruction at Interfaces in Ultrathin $\text{La}_{0.67}\text{Sr}_{0.33}\text{MnO}_3$ Films. *Phys. Rev. Lett.* **100**, 137401 (2008).
- Pesquera, D. et al. Surface symmetry-breaking and strain effects on orbital occupancy in transition metal perovskite epitaxial films. *Nat. Commun.* **3**, 1189 (2012).
- Moon, E. J. et al. Effect of Interfacial Octahedral Behavior in Ultrathin Manganite Films. *Nano Lett.* **14**, 2509–2514 (2014).
- Cui, B. et al. Manipulation of Electric Field Effect by Orbital Switch. *Adv. Funct. Mater.* **26**, 753–759 (2016).
- Bardeen, J., Cooper, L. N. & Schrieffer, J. R. Theory of Superconductivity. *Phys. Rev.* **108**, 1175–1204 (1957).
- Husanu, M.-A. et al. Electron-polaron dichotomy of charge carriers in perovskite oxides. *Commun. Phys.* **3**, 62 (2020).
- Yamada, H. et al. Ferroelectric control of a Mott insulator. *Sci. Rep.* **3**, 2834 (2013).
- Cancellieri, C. et al. Polaronic metal state at the $\text{LaAlO}_3/\text{SrTiO}_3$ interface. *Nat. Commun.* **7**, 10386 (2016).
- Verdi, C., Caruso, F. & Giustino, F. Origin of the crossover from polarons to Fermi liquids in transition metal oxides. *Nat. Commun.* **8**, 10386 (2017).
- Strocov, V. N. Intrinsic accuracy in 3-dimensional photoemission band mapping. *J. Electron Spectrosc. Relat. Phenom.* **130**, 65–78 (2003).
- Strocov, V. N. et al. Soft-X-ray ARPES facility at the ADDRESS beamline of the SLS: concepts, technical realisation and scientific applications. *J. Synchrotron Radiat.* **21**, 32–44 (2014).
- Shin, Y. J. et al. Interface Control of Ferroelectricity in an $\text{SrRuO}_3/\text{BaTiO}_3/\text{SrRuO}_3$ Capacitor and its Critical Thickness. *Adv. Mater.* **29**, 1602795 (2017).
- Xu, R. et al. Reducing Coercive-Field Scaling in Ferroelectric Thin Films via Orientation Control. *ACS Nano* **12**, 4736–4743 (2018).
- Jo, J. Y., Kim, Y. S., Noh, T. W., Yoon, J.-G. & Song, T. K. Coercive fields in ultrathin BaTiO_3 capacitors. *Appl. Phys. Lett.* **89**, 232909 (2006).
- Chirila, C. F. et al. Controlling polarization direction in epitaxial $\text{Pb}(\text{Zr}_{0.2}\text{Ti}_{0.8})\text{O}_3$ films through Nb (n-type) and Fe (p-type) doping. *Sci. Rep.* **12**, 755 (2022).
- Teodorescu, C. M. Self-consistently derived sample permittivity in stabilization of ferroelectricity due to charge accumulated at interfaces. *Phys. Chem. Chem. Phys.* **24**, 5419–5430 (2022).
- Teodorescu, C. M. Ferroelectricity in thin films driven by charges accumulated at interfaces. *Phys. Chem. Chem. Phys.* **23**, 4085–4093 (2021).
- Pintilie, L. et al. Polarization induced self-doping in epitaxial $\text{Pb}(\text{Zr}_{0.20}\text{Ti}_{0.80})\text{O}_3$ thin films. *Sci. Rep.* **5**, 14974 (2015).

29. Liao, Z. et al. Origin of the metal-insulator transition in ultrathin films of $\text{La}_{2/3}\text{Sr}_{1/3}\text{MnO}_3$. *Phys. Rev. B* **92**, 125123 (2015).
30. Merten, S., Bruchmann-Bamberg, V., Damaschke, B., Samwer, K. & Moshnyaga, V. Jahn-Teller reconstructed surface of the doped manganites shown by means of surface-enhanced Raman spectroscopy. *Phys. Rev. Mater.* **3**, 060401(R) (2019).
31. Lev, L. L. et al. Fermi Surface of Three-Dimensional $\text{La}_{1-x}\text{Sr}_x\text{MnO}_3$ Explored by Soft-X-Ray ARPES: Rhombohedral Lattice Distortion and its Effect on Magnetoresistance. *Phys. Rev. Lett.* **114**, 237601 (2015).
32. Horiba, K. et al. Isotropic Kink and Quasiparticle Excitations in the Three-Dimensional Perovskite Manganite $\text{La}_{0.6}\text{Sr}_{0.4}\text{MnO}_3$. *Phys. Rev. Lett.* **116**, 076401 (2016).
33. Luttinger, J. M. Fermi Surface and Some Simple Equilibrium Properties of a System of Interacting Fermions. *Phys. Rev.* **119**, 1153–1163 (1960).
34. Jia, C.-L. et al. Direct Observation of Continuous Electric Dipole Rotation in Flux-Closure Domains in Ferroelectric $\text{Pb}(\text{Zr,Ti})\text{O}_3$. *Science* **331**, 1420–1423 (2011).
35. Matt, C. E. et al. Direct observation of orbital hybridisation in a cuprate superconductor. *Nat. Commun.* **9**, 972 (2018).
36. Björnsson, P. et al. Lattice and charge excitations in $\text{La}_{1-x}\text{Sr}_x\text{MnO}_3$. *Phys. Rev. B* **61**, 1193–1197 (2000).
37. Hartinger, C., Mayr, F., Loidl, A. & Kopp, T. Polaronic excitations in colossal magnetoresistance manganite films. *Phys. Rev. B* **73**, 024408 (2006).
38. Asamitsu, A. & Tokura, Y. Hall effect in $\text{La}_{1-x}\text{Sr}_x\text{MnO}_3$. *Phys. Rev. B* **58**, 47–50 (1998).
39. Fröhlich, H. Electrons in lattice fields. *Adv. Phys.* **3**, 325–361 (1954).
40. Rosenfelder, R. & Schreiber, A. W. On the best quadratic approximation in Feynman's path integral treatment of the polaron. *Phys. Lett. A* **284**, 63–71 (2001).
41. Hahn, T., Klimin, S., Tempere, J., Devreese, J. T. & Franchini, C. Diagrammatic Monte Carlo study of Fröhlich polaron dispersion in two and three dimensions. *Phys. Rev. B* **97**, 134305 (2018).
42. Mishchenko, A. S., Prokofev, N. V. & Sakamoto, A. Diagrammatic quantum Monte Carlo study of the Fröhlich polaron. *Phys. Rev. B* **62**, 6317 (2000).
43. Sluka, T., Tagantsev, A. K., Bednyakov, P. & Setter, N. Free-electron gas at charged domain walls in insulating BaTiO_3 . *Nat. Commun.* **4**, 1808 (2013).
44. Grimaldi, C., Pietronero, L. & Strässler, S. Nonadiabatic Superconductivity: Electron-Phonon Interaction Beyond Migdal's Theorem. *Phys. Rev. Lett.* **75**, 1158–1161 (1995).
45. Giannozzi, P. et al. Advanced capabilities for materials modelling with Quantum ESPRESSO. *J. Phys. Condens. Matter* **29**, 465901 (2017).
46. Giannozzi, P. et al. QUANTUM ESPRESSO: a modular and open-source software project for quantum simulations of materials. *J. Phys. Condens. Matter* **21**, 395502 (2009).
47. van Setten, M. J. et al. The PseudoDojo: Training and grading a 85 element optimized norm-conserving pseudopotential table. *Comput. Phys. Commun.* **226**, 39–54 (2018).
48. Dorin, R., Filip, L. D., Pintilie, L., Butler, K. T. & Plugaru, N. Designing functional ferroelectric interfaces from first-principles: dipoles and band bending at oxide heterojunctions. *N. J. Phys.* **21**, 113005 (2019).

Acknowledgements

This work was funded by the Romanian UEFISCDI Agency under Contract No. PN-III-P4-ID-PCCF2016-0047. D.G.P. acknowledges funding from PN-III-P1-1.1-TE-2021-

0136 (TE50/2022) project. M.-A.H. acknowledges the support of the Swiss Excellence Scholarship grant ESKAS-no. 2015.0257 and of the Romanian UEFISCDI Agency under Contract No. PN-III-P4-ID-PCE-2020-2540. SX-ARPES measurements were performed at the ADDRESS beamline from Swiss Light Source under the proposals no. 20151375, 20160516 and 20170810. ASM acknowledge JST CREST Grant Number JPMJCR1874, Japan. F.B. acknowledges funding from Swiss National Science Foundation under Grant Agreement No. 200021_146890 and from European Community's Seventh Framework Programme (FP7/2007-2013) under Grant Agreement No. 290605 (PSIFELLOW/COFUND). The fee for open access publication was supported from the project 35PFE/2021, funded by the Romanian Ministry of Research, Innovation and Digitization.

Author contributions

M.A.H. elaborated the idea of the experiments with input from V.N.S. and L.P. L.E.H. prepared the samples assisted by L.P. M.A.H., D.G.P., F.B., L.L.L. performed the SX-ARPES measurements assisted by V.N.S. and T.S., I.P. performed XRD analyses, R.N. and C.I. performed TEM investigations, M.A.H. and L.D.F. performed ab-initio calculations. A.S.M. provided the picture of coexisting 2D and 3D polarons. M.A.H., D.G.P. and F.B. processed the photoemission data assisted by V.N.S. and C.M.T. M.A.H. and V.N.S. wrote the manuscript with input from all the authors.

Competing interests

The authors declare no competing interests

Additional information

Supplementary information The online version contains supplementary material available at <https://doi.org/10.1038/s42005-022-00983-3>.

Correspondence and requests for materials should be addressed to Marius Adrian Husanu or Vladimir N. Strocov.

Peer review information *Communications Physics* thanks Zhonghao Liu and the other, anonymous, reviewer(s) for their contribution to the peer review of this work. Peer reviewer reports are available.

Reprints and permission information is available at <http://www.nature.com/reprints>

Publisher's note Springer Nature remains neutral with regard to jurisdictional claims in published maps and institutional affiliations.



Open Access This article is licensed under a Creative Commons

Attribution 4.0 International License, which permits use, sharing, adaptation, distribution and reproduction in any medium or format, as long as you give appropriate credit to the original author(s) and the source, provide a link to the Creative Commons license, and indicate if changes were made. The images or other third party material in this article are included in the article's Creative Commons license, unless indicated otherwise in a credit line to the material. If material is not included in the article's Creative Commons license and your intended use is not permitted by statutory regulation or exceeds the permitted use, you will need to obtain permission directly from the copyright holder. To view a copy of this license, visit <http://creativecommons.org/licenses/by/4.0/>.

© The Author(s) 2022